

Interstellar Reddening for Planetary Nebulae Toward Galactic Bulge

Yong-Ik Byun

*Institute of Astronomy, National Central University,
Chung-Li, Taiwan 320, R.O.C.*

(Received April 29, 1996)

Spectrophotometric data for six planetary nebulae in the direction of the galactic bulge were used to derive the properties of the interstellar reddening for this region. The observed nebular continuum was compared with theoretically predicted nebular continuum and the interstellar reddening was evaluated from the differences. The derived reddening function for each nebula shows generally good agreement with the Whitford reddening law in long wavelengths of visible region. However, there exist significant deviations from the standard law in ultraviolet, which may be explained by either different composition or different size distribution of the dust grains lying toward the galactic center. A rough estimate suggests $R = 1.5 \sim 2.0$, which is significantly smaller than the standard value of $R = 3$.

PACS. 95.75.Fg - Spectroscopy and spectrophotometry.

PACS.98.58.Li - Planetary nebulae.

PACS.98.58.Ca - Interstellar dust grains.

I. Introduction

Determination of interstellar reddening is important in many fields of astronomy. Interstellar dust grains, which are responsible for the reddening effect, obscure the stars and other sources of radiation and distort the information on the intrinsic properties of the radiation sources. Before we can study the true nature of an astronomical object the effect of interstellar matter lying in the line of sight needs to be understood. Equally importantly, the absorption and scattering of light contain the information needed to improve our understanding of dust grains themselves as well as their contribution to the physical processes in the general interstellar medium.

The optical properties of small solid particles called dust grains are rather well known. They scatter and absorb radiation in interstellar space and, as a result of the heating effect of the absorption, produce radiation at wavelengths of much greater than those of the absorbed light. This phenomenon is known as *extinction*. The reddening of the incident light is caused by the strong wavelength dependence of this process. The composition of dust grains as well as their size distribution determines the details of wavelength dependence in interstellar extinction [1].

The study of planetary nebulae also needs a correction for the interstellar reddening before any other analysis including the abundance determination. In addition, the reddening information can be used to derive the distances to the planetary nebulae in the form of a reddening-distance relation. The distance is perhaps the most important single parameter for planetary nebulae and we have only a few very poor indicators.

There are several known ways to determine the reddening of a planetary nebula (for review, see [2]). They are; (a) The ratio of the radio continuum flux density with the $H\beta$ flux. From the theory of nebular continuum and recombination line formation, we can calculate the expected ratio of radio continuum flux density to $H\beta$ as a function of electron temperature and helium abundance. Since the observed radio flux density is free from interstellar reddening, the comparison between theoretically predicted $H\beta$ flux and the observed $H\beta$ flux is used to determine the amount of extinction. (b) Ratios of the nebular H Balmer lines (Balmer decrements). The relative intensity of the hydrogen Balmer emission lines, such as $H\alpha$, to $H\beta$, $H\gamma$ to $H\beta$, etc., depends only on the electron temperature of the nebula. But this dependency is very weak and can be assumed to be the same for all nebulae. The selective interstellar absorption distorts the theoretical decrements and makes them significantly steeper. The comparison between the expected and observed decrements gives the reddening. The ratio of nebular He II lines $\lambda 4686\text{\AA}$ and $\lambda 1640\text{\AA}$ can be used in the same way. The ratio of lines arising from a common upper level, such as forbidden lines of [S II] $\lambda 10680\text{\AA}$ and [S II] $\lambda\lambda 4068\text{\AA}, 4076\text{\AA}$, is also an indicator of interstellar reddening. (c) The strength of an absorption feature at 2200\AA in the observed nebular UV continuum. The $\lambda 2200\text{\AA}$ peak is a well known feature related to the effect of a surface charge resonance on small graphite grains. By assuming that the continuum is intrinsically continuous, the extinction can be estimated from the depth and shape of the absorption.

In the present paper, we introduce a new method of determining the interstellar reddening for planetary nebulae. Using the spectrophotometric data of six planetary nebulae toward, and probably in, the galactic bulge, the reddening is derived from a direct comparison between the observed and theoretically predicted nebular continuum emission. Section II describes the observation and data reduction procedures. The construction of model nebular continuum is presented in section III. The interstellar reddening of each planetary nebula is derived in section IV. Section V discusses the results and their implications.

II. Observation and data reduction

The sample planetary nebulae include 349+4.1, 355-2.3, 000-1.6, 002-2.4 KFL#3, and 006-3.3. They were chosen from the nebulae in Baade's Window, which is in the direction of the galactic bulge. Considering the strong concentration of planetary nebulae toward the galactic center, it is most likely that these planetary nebulae are actually within the galactic bulge and have similar distances. Basic properties of the six observed planetary nebulae are given in Table I. The identification follows Perek and Kohoutek (PK) designation [3] with an exception of KFL#3, which is named after [4]. PK designation is a combination of galactic coordinates for longitude and latitude.

Observations were made with the Double Beam Spectrograph (DBS, [5]) at the Australian National University 2.3 m telescope at the Siding Spring Observatory. The DBS was used with 300 lines/mm gratings in the red and blue arms, which provided a wavelength

TABLE I. Basic properties of the observed planetary nebulae

PK Desig.	Name	R. A. (1950) Dec.			Size(")	Velocity (km/s)
349+4.1	M 2-4	16 57 47.7	-34 45 17		1.2	- 175.8
355-2.3	H1-32	17 42 47.4	-34 02 37		0.6	- 179.1
000- 1.6	M2-20	17 51 13.6	-29 35 38		5.1	+85.2
002-2.4	M2-23	17 58 32.7	-28 25 46		7.6	+234.7
KFL#3		17 59 38.3	-31 24 03		12.2	+200.0
006-3.3	M2-31	18 10 10.5	-25 30 56		6.4	+168.7

coverage of 3500Å to 7500Å. The red and blue spectrum is separated by a dichroic beam splitter cutting at 5500Å. The DBS system had two different kinds of cathodes. On the blue arm is mounted a large format Photon Counting Array (PCA) with an S-20 photocathode on a quartz substrate, whereas an NEA Ga-As cathode with similar large format photon counting system is used for the red arm. Two Charge-Coupled-Devices (CCD) are attached at the end of each PCA.

Observations of the target objects were accompanied with exposures of a He-Ar arc lamp. Two or more of Oke and Gunn spectrophotometric flux standard stars [6] were observed every night. The exposure times were typically 1000 sec. However, since the PCA saturates on bright lines, it was also necessary to take additional 1000 sec exposures with the telescope defocused, and the slit narrowed in order to obtain accurate relative fluxes for the brighter lines. In some cases, neutral density filters were used for the additional exposures.

The FIGARO package developed at the Anglo-Australia Observatory was used for the data reduction. Since the data fell on four different CCDs, each CCD had to be reduced separately, and then combined into a single spectrum. The reduction process consisted of flat fielding, data extraction, wavelength linearisation, sky subtraction, reduction to flux, merging of CCDs and summing of rows to extract individual spectra.

Flat fielding is to correct the data for small scale variations of instrumental sensitivity across the CCDs. Quartz lamp inside DBS was used to obtain flat field frames. For direct imaging data, the flat fielding is usually done by simply dividing the data frames by a normalized flat-field frame. The flat field frames for spectroscopic data, however, are subject to the spectral energy distribution of the flat-field lamp. This effect needs to be removed before their application to the data frames. The raw flat fields are collapsed in the y-direction (dispersion axis) for each CCD to represent the large scale spectral variation caused by the flat field lamp. The raw flat fields are then divided by a spline fit to this collapsed spectrum. The resulting frame is normalized by its mean and used for the flatfielding of the data frames. There was also a suspicion that the lamp illumination may not be uniform in the y-direction, but the examination of flat field after collapse in the x-direction (wavelength axis) showed no large scale variation along the y-direction.

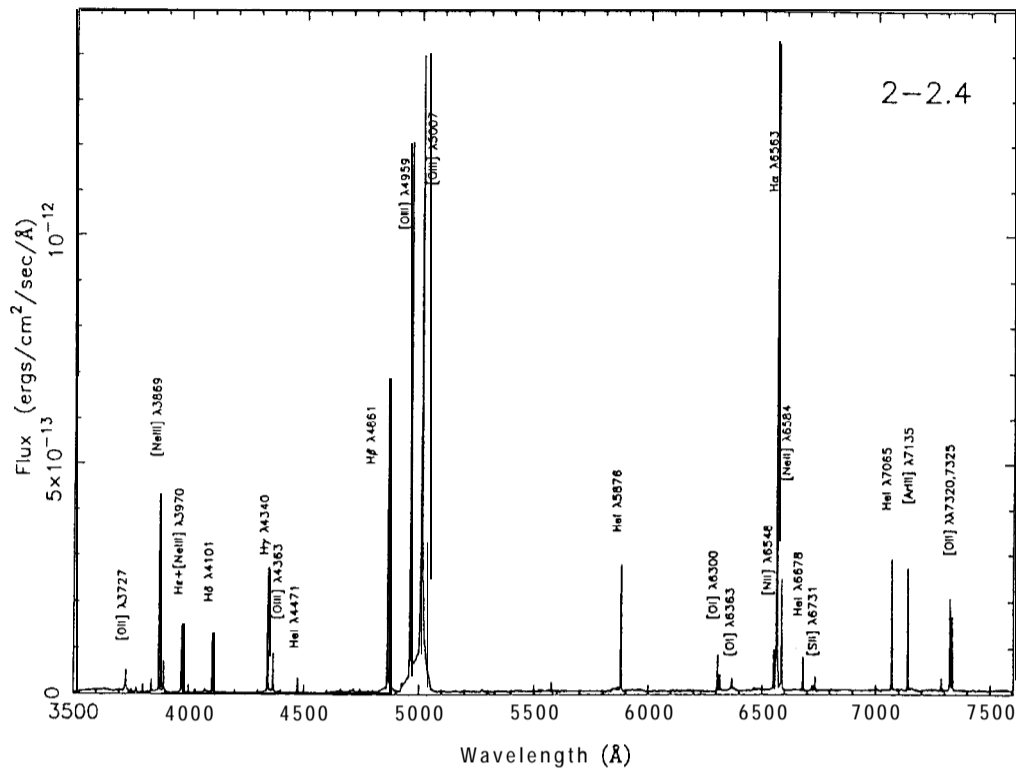


FIG.1. Spectrum of planetary nebula 2-2.4. Major emission lines are indicated with their rest frame wavelengths. Some strong lines are blended and/or saturated. For these lines, the exposures with neutral density filter or with telescope defocusing were used for further analysis.

After flat-fielding, each frame was wavelength-calibrated and scrunched to uniform dispersion in wavelength. Although there is no clear indication of a significant change in the wavelength-channel relationship across the image, a two-dimensional scrunching was applied because our objects were all extended sources. Good fits for every cross-section of the He-Ar arc image were derived and applied to each cross-section of the data image separately. The spectral image was then extracted into an one-dimensional spectrum.

Next step was to remove the sky contribution to the object spectrum. This is usually done by extracting separate sky spectrum from each frame. However the selection of sky region was not trivial in our case: since galactic bulge is very crowded region. The sky area in the dispersion axis was selected by careful inspections of image display as well as of the intensity distribution along the dispersion axis after collapsing the data along the wavelength axis.

The atmospheric extinction was corrected according to the AAO extinction coefficient table. The final flux calibration was done against the Oke and Gunn flux standard white dwarf stars.

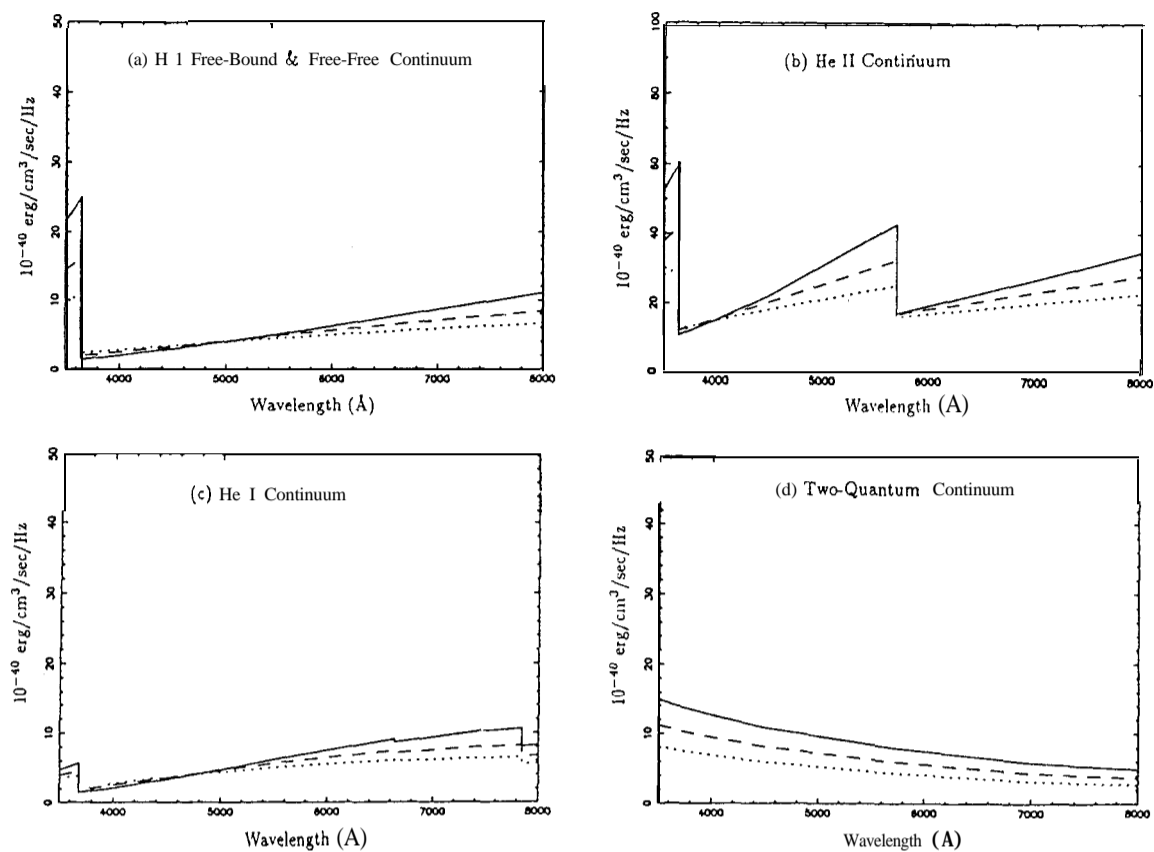


FIG. 2. Theoretical nebular continuum emission for various radiation processes. Three cases of electron temperatures are considered. Solid lines correspond to 10000°K , broken lines to 15000°K , and dotted lines to 20000°K .

Fig. 1 shows an example of fully reduced nebular spectrum. There are two kinds of typical nebular emission lines. First, those lines formed by a recombination process of ions through the capture of an electron by a positively charged ion, for example hydrogen and helium lines. Secondly, there are strong emission lines formed by collisional excitation of an atom or ion followed by spontaneous radiation. This mechanism called forbidden transition is especially dominant in nebular spectra because of their low density. These lines are indicated with square brackets.

The spectrum of planetary nebulae consist of not only line emissions but also continuum emission. Both reflect the physical conditions in the nebula such as the electron density, temperature, chemical abundance, the properties of the central star, etc. In the present paper, we are mainly interested in the nebular continuum emission, which will be used to derive the extinction toward these planetary nebulae.

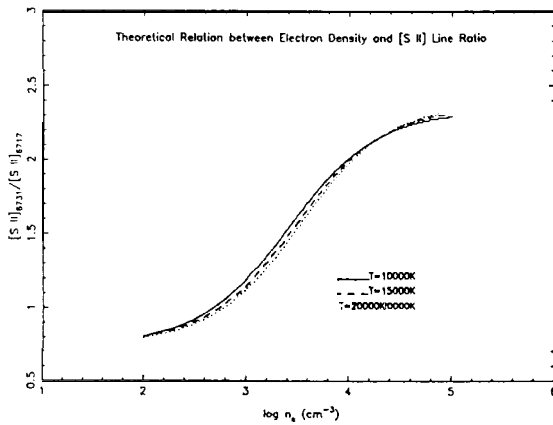


FIG. 3. Relation between electron density and [S II] line ratio. Three cases of electron temperatures are considered.

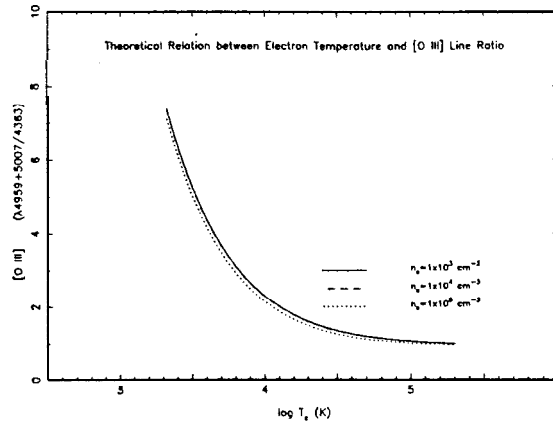


FIG. 4. Relation between electron temperature and [O III] line ratio. Three cases of electron densities are considered.

III. Nebular continuum

The nature of nebular continuum radiation is well known since the radiation is mostly due to interactions between electrons and hydrogen and helium ions except in the far infrared region where dust grains play an important role. In order to compare with the observed continuum, a model continuum needs to be constructed from radiation theories. Atomic processes responsible for the continuum emission from far ultraviolet to the near infrared are described below.

Free-bound and free-free emission of H I, He I, and He II; The continuous spectrum of planetary nebulae below the Balmer limit of hydrogen ($\lambda < 3646\text{\AA}$) results from the capture of free electrons by protons into the level $n=2$ of neutral hydrogen (free-bound transition). On the other hand, the continuous spectrum on the long wavelength side of the Balmer limit originates firstly from free-free transitions of electrons in the field of a proton, and secondly from the capture of free electrons by protons into the levels $n = 3, 4, 5 \dots$ of neutral hydrogen, during which Paschen ($\lambda < 820281$) and higher series continuum photons are emitted. The basic principle of this mechanism is also applied to the neutral and ionized helium.

Two-quantum emission process; this is a downward transition of an atom during which two photons are emitted. The probability of such transition is extremely small in most cases, but for certain metastable levels the probability is sufficiently large to be comparable with that of forbidden transitions. The frequencies of those emitted quanta during two-quantum transitions are arbitrary and therefore form a continuum. The total energy released equals the excitation energy of the original level.

For neutral hydrogen, the two-quantum emission takes place in transitions from the metastable $2S_{1/2}$ to the ground state $1S_{1/2}$. After a capture of a free electron, the atom experiences cascade transitions downwards until it reaches the $n=2$ state. When it passes

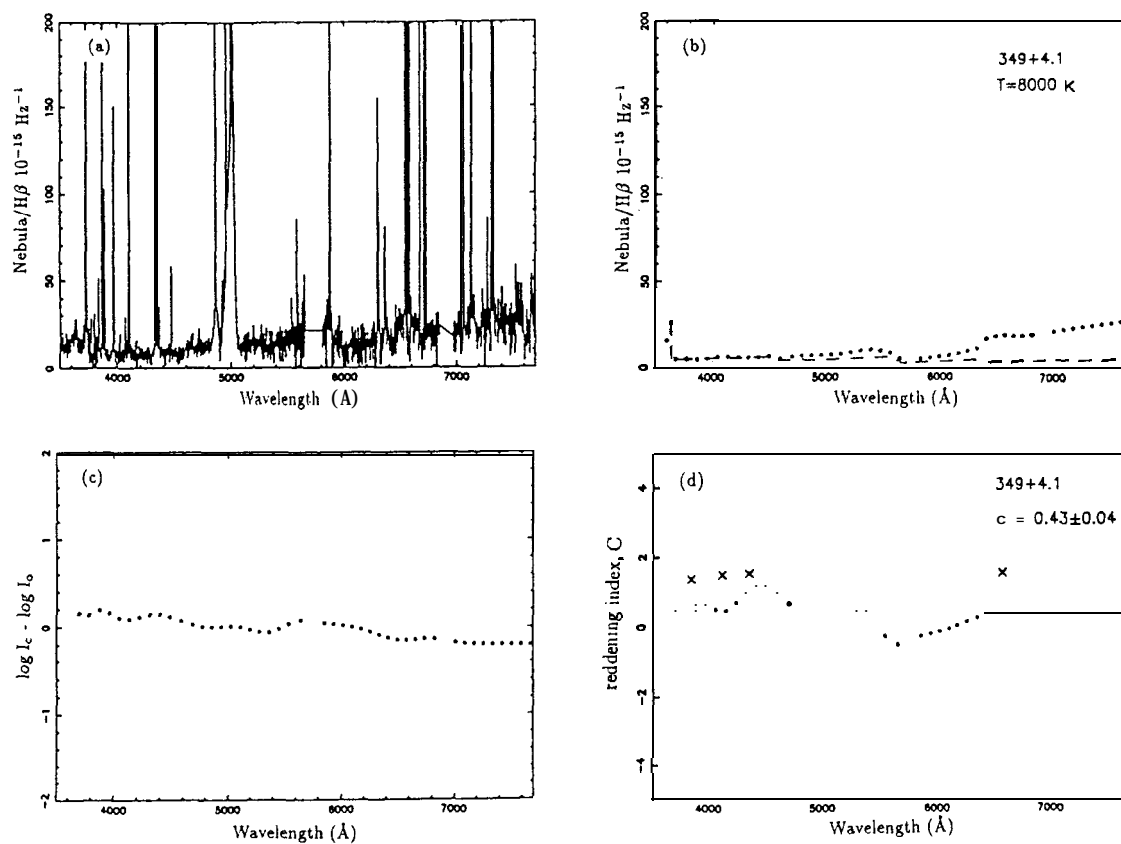


FIG. 5. Evaluation of the interstellar reddening for 349 + 4.1. (a) the observed continuum of planetary nebula. (b) comparison of the fitted observed continuum (dotted line) with theoretically predicted continuum (broken line). (c) logarithmic difference normalized at $\lambda 4861\text{Å}$. (d) the distribution of reddening as a function of wavelength (dotted line). The reddening was obtained by dividing the logarithmic difference in (c) by Whitford reddening function. The mean reddening constant c was obtained from the flat part in longer wavelength region marked by a horizontal line. c value and associated error are given in the diagram. The reddening values from Balmer decrements are indicated by crosses.

the 2P level it must continue on its way to the ground state by emitting a Lyman- α photon. A certain fraction of the atoms, however, reach the 2S level and consequently undergo two-quantum emission. Considering the ratio of the statistical weights of the 2S and 2P levels, one may conclude that nearly one third of the H atoms in recombination processes reach the ground state by means of two-quantum emission. The two-quantum transitions also exist for helium atoms since both neutral helium and ionized helium have metastable 2S levels. Because of the lower helium abundance in nebulae as well as their small emission coefficients, this process is much less important than the hydrogen twoquantum emission (except in the far-ultraviolet).

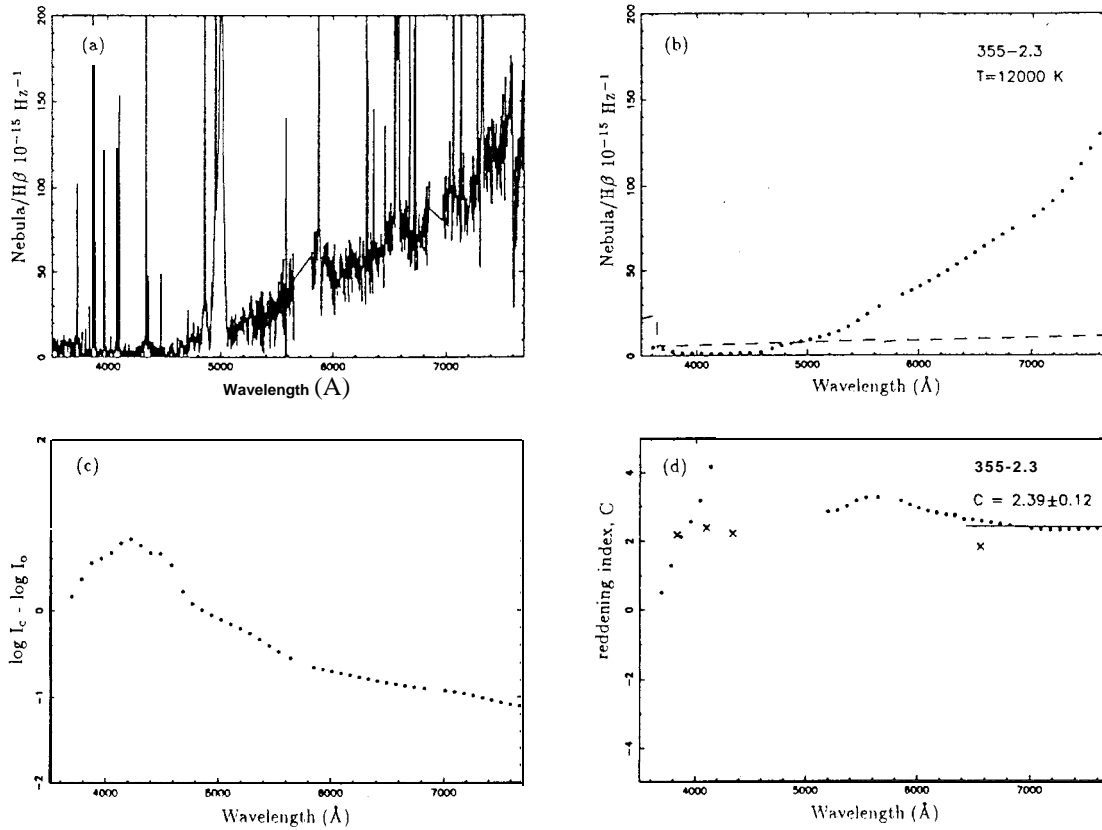


FIG. 6. Same as Fig. 5, but for planetary nebula 355-2.3.

Above processes for continuum emission is a strong function of electron temperature. Fig. 2 demonstrates the variation of emission coefficients for each process at three different electron temperatures. The total nebular continuum emission is given by

$$\gamma_{total} = y(M) + 0.1\gamma(\text{HeII}) + 0.05\gamma(\text{HeII}) + 0.33\gamma(2q), \quad (\text{I})$$

assuming $\text{H}\epsilon^+/\text{H}\alpha = 0.05$ and $\text{He}^+/\text{H} = 0.1$. Since the continuum emission is proportional to the square of the density integrated over the volume of the nebula, the comparison of theory with observation is always made between the predicted and observed ratio of continuum emission to a spectral line. The theoretical H β line intensities [7] are interpolated to estimate the H β intensities at various electron temperatures, which is then used for the comparison with the observed continuum in the next section.

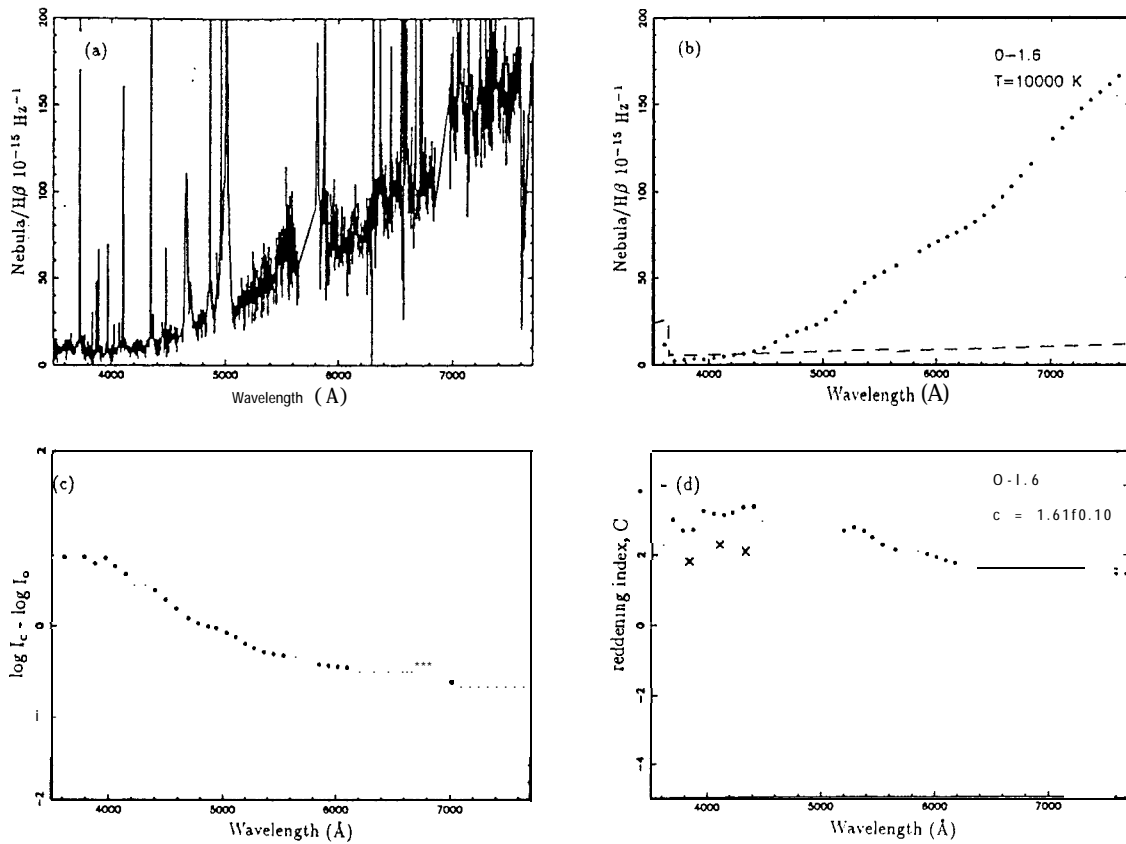


FIG. 7. Same as Fig. 5, but for planetary nebula 000-1.6.

IV. Determination of interstellar reddening

IV-1. Determination of electron temperature and density

There are several forbidden emission lines, which are strong functions of electron temperature and density in planetary nebulae. Ionized oxygen and sulfur are often used as density indicators because they radiate density-sensitive emission lines. However the $[\text{O II}]\lambda\lambda 3726, 3729\text{\AA}$ doublet is not resolved in our spectra, so $[\text{S II}]\lambda\lambda 6717, 67318$, red doublet was used to derive the electron density for our sample nebulae. To establish the relationship between $[\text{S II}]$ line ratio and electron density, theoretical calculations were performed using the package MAPPINGS (see [8] and [9] for details). Fig. 3 shows the dependence of the line ratio $[\text{S II}]\lambda 6731/[\text{S II}]\lambda 6717$ on electron density. For the expected range of planetary nebular temperatures, the ratio of these lines is only a weak function of temperature.

The electron temperature T_e can be determined by some temperature dependent lines such as $[\text{O III}]$ or $[\text{N II}]$ forbidden lines. We lack an observation of the weak $[\text{N II}]\lambda 5754\text{\AA}$ auroral line and consequently cannot derive $T_e/[\text{N II}]$. But for all of the observed planetary nebulae we have well-determined intensities for $[\text{O III}]\lambda 4363\text{\AA}$ so that accurate

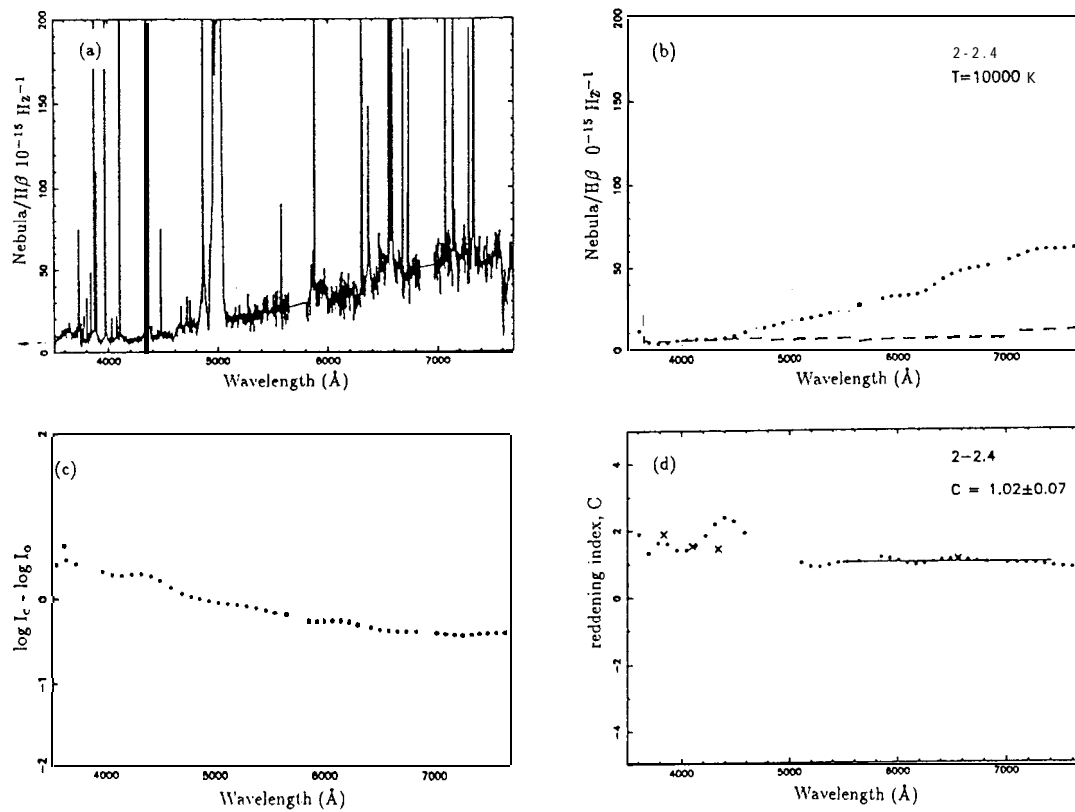


FIG. 8. Same as Fig. 5, but for planetary nebula 002-2.4.

[0 III] electron temperatures can be assessed. Instead of using empirically established formulae, MAPPINGS package was used again to set up the theoretical relationship between electron temperature and [0 III] line ratio $(X4959 + X5007) / X4363$, which is illustrated in Fig. 4. As shown in the figure, [0 III] line ratio has very weak dependence on electron density.

The line intensities were measured from fully reduced spectra using a FIGARO routine GAUSS. Consequently, each theoretical relationship was applied to the observed planetary nebular emission lines after a preliminary reddening correction based on the accurately determined H α intensities, where we assume the true dereddened value to be 285 [10]. The derived electron temperatures and densities are listed in Table II.

IV-2. Interstellar reddening

In this section we compare the observed continuum of each planetary nebula with theoretically predicted continuum of corresponding electron temperature, as an attempt to determine the interstellar reddening. The observed continuum was first fitted into a smooth line and divided by measured H β line intensity. The difference of the observed continuum from the theoretical counterpart is assumed to be resulted solely from the interstellar reddening. The interstellar reddening is defined as

TABLE II. Electron temperatures and densities of the observed planetary nebulae

PK Desig.	Te [O III]	ne [S II]
349 + 4.1	8200 K	$3.1 \times 10^3 \text{ cm}^{-3}$
355 - 2.3	11400	3.5×10^3
000 - 1.6	9000	3.2×10^3
002 - 2.4	10500	6.5×10^4
KFL#3	12600	1.0×10^2
006 - 3.3	11500	3.5×10^3

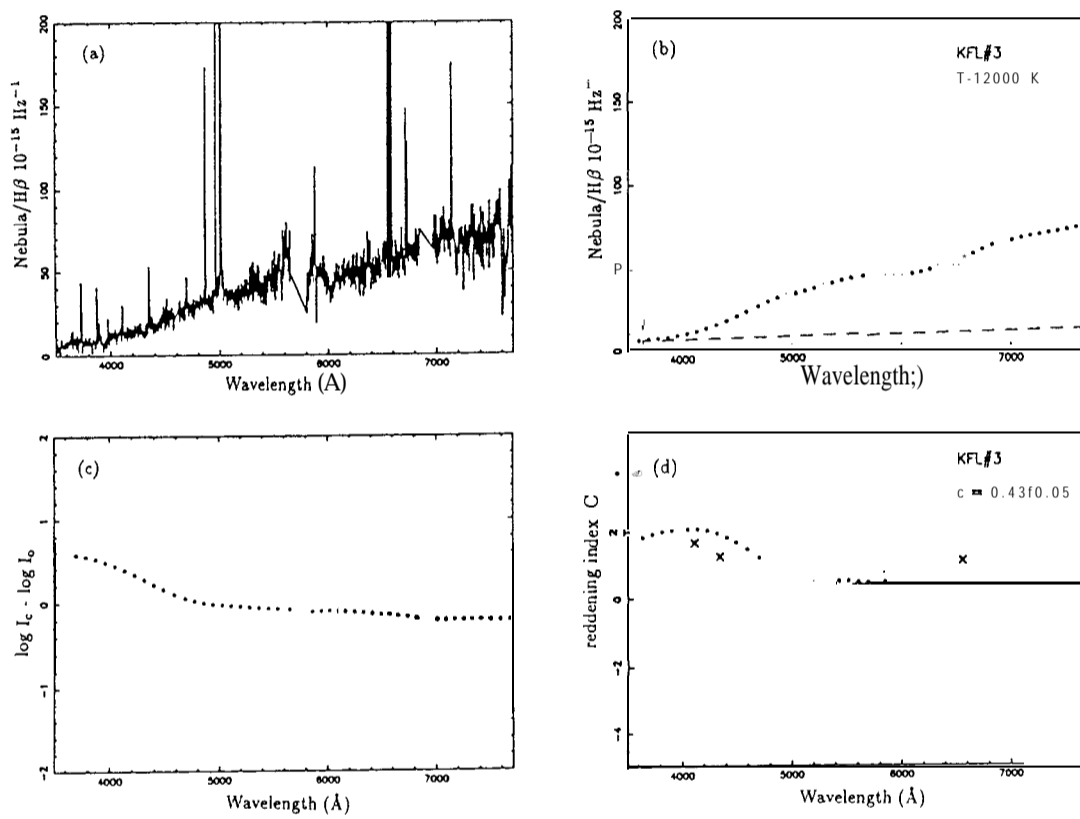


FIG. 9. Same as Fig. 5, but for planetary nebula KFL#3.

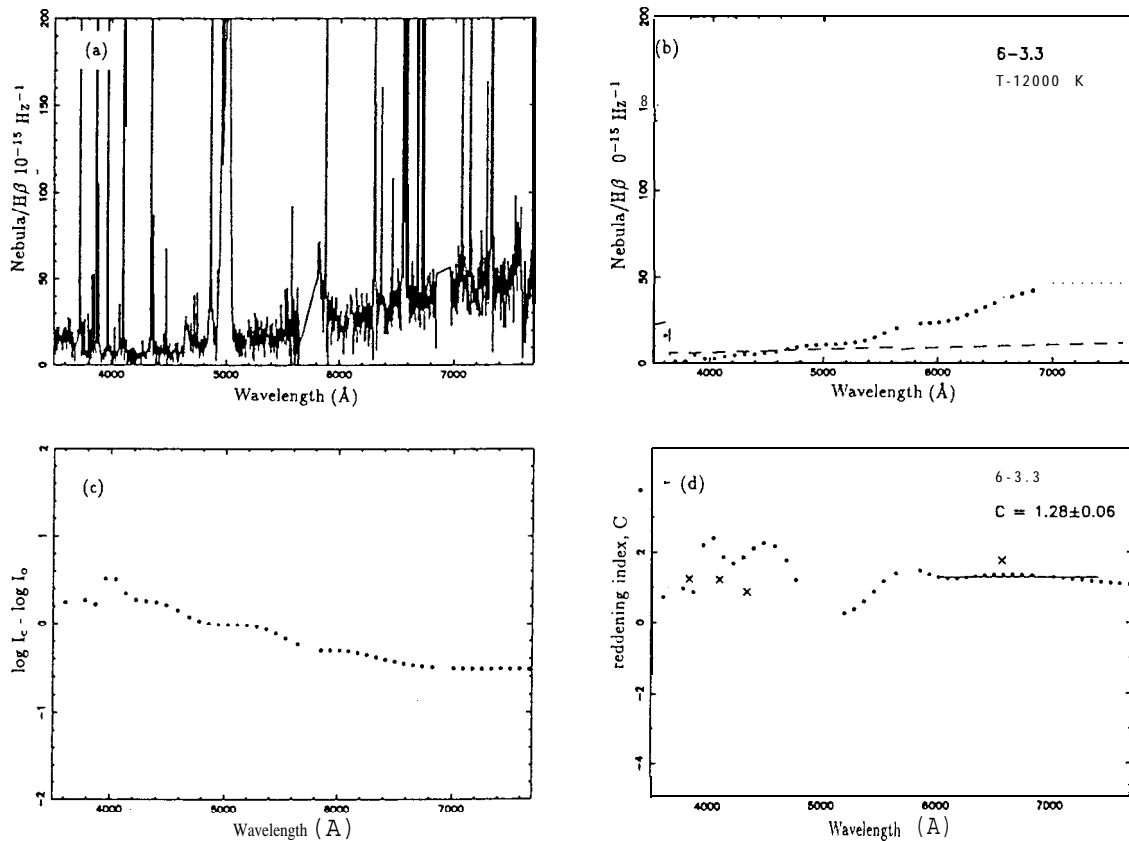


FIG. 10. Same as Fig. 5, but for planetary nebula 006-3.3.

$$\log I_c = \log I_o + c \cdot f_\lambda, \quad (2)$$

where the values of interstellar reddening function f_λ are taken from Whitford[11] and normalized at $H\beta$. Therefore the logarithmic difference gives the reddening constant c when it is divided by the Whitford reddening function. The procedures and results for the present sample planetary nebulae are illustrated in Fig. 5 to Fig. 10. The mean reddening constant for each nebula was derived from the flat part of the curve (usually long wavelength side) given in the last panels of Fig. 5 to Fig. 10. The reddening constant values around $\lambda 4861\text{\AA}$ were masked out since this region is divided by values close to zero.

In order to compare our results with other methods, we derived the reddening constants independently from Balmer decrement using $H\alpha$, $H\gamma$ and H_{10} emission lines. The relative intensities of these lines to $H\beta$, line were used for the determination of the interstellar extinction. The theoretical Balmer decrement was taken from [10] and the Whitford reddening law [11] was used. The derived reddening constant values are indicated in the last panels of Fig. 5 to Fig. 10 to be compared with the values derived from the continuum method. Except 349 ± 4.1 , they generally show a good agreement at least in the long wavelength regions.

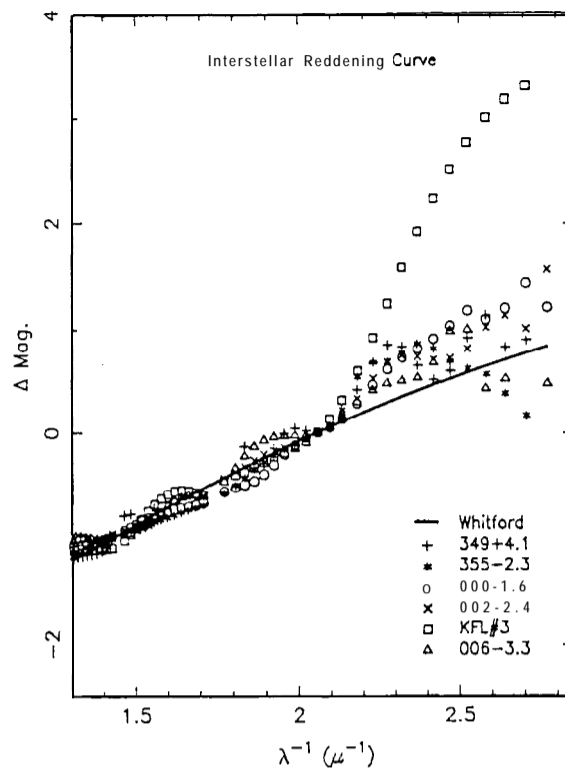


FIG.11. The interstellar reddening curves for the observed planetary nebulae are compared with the standard Whitford reddening law. They tend to be steeper in ultraviolet and rather flatter in longer wavelength domain.

If the Whitford reddening function is valid for all of these object, we should expect a constant reddening index along the whole wavelength range. However the distribution of reddening indices do not show such constancy for most sample planetary nebulae especially in shorter wavelength domain. This suggests that there are deviations from the standard Whitford reddening function. The reddening functions derived from nebular continuum are listed in Table III and visually compared with Whitford reddening in Fig. 11. As shown in the figure, there is more or less good agreement with Whitford function in the longer wavelength side of $H\beta$ line. However significant dispersions exist in blue wavelength region. An averaged curve, rejecting the points greater than 2σ , suggests that there is a general trend that the reddening function gets steeper at short wavelengths and flatter at longer wavelengths.

It is not clear what causes the large difference in reddening function among the sample nebulae at short wavelengths. We note that such behavior may reflect different properties of dust within each of these planetary nebulae. After all, the reddening does not only arise from the dust clouds lying in the line-of-sight to a nebula, but also from the dust within the nebula. There are indications which suggest this may be the case. For instance, KFL#3 shows much larger deviation than any other sample nebulae in the short wavelength domain. According to our analysis, this nebula shows very abnormal electron density which is one

TABLE III. The derived mean reddening functions for the observed planetary nebulae

wavelength (Å)	Whitford 349+4.1	355-2.3	000-1.6	002-2.4	KFL#3	006-3.3	
3600	0.34	0.92	0.27	0.47	0.65	2.85	0.22
3700	0.31	0.35	0.07	0.57	0.40	1.29	0.03
3800	0.28	0.36	0.17	0.46	0.46	1.28	0.21
3900	0.25	0.45	0.24	0.45	0.38	1.16	0.23
4000	0.22	0.30	0.26	0.45	0.30	1.06	0.44
4100	0.20	0.21	0.31	0.38	0.28	0.94	0.32
4200	0.17	0.24	0.35	0.34	0.29	0.80	0.22
4300	0.14	0.33	0.32	0.30	0.30	0.65	0.20
4400	0.12	0.34	0.28	0.24	0.27	0.49	0.19
4500	0.09	0.26	0.27	0.17	0.20	0.35	0.16
4600	0.07	0.15	0.20	0.10	0.12	0.22	0.11
4700	0.04	0.06	0.08	0.05	0.06	0.12	0.06
4800	0.02	0.01	0.02	0.01	0.02	0.04	0.01
4900	-0.01	0.00	-0.01	-0.01	-0.01	-0.02	-0.00
5000	-0.03	0.02	-0.04	-0.04	-0.04	-0.05	-0.01
5100	-0.05	0.00	-0.06	-0.08	-0.05	-0.07	-0.01
5200	-0.07	-0.06	-0.09	-0.12	-0.07	-0.09	-0.01
5300	-0.10	-0.13	-0.12	-0.16	-0.08	-0.12	-0.03
5400	-0.12	-0.11	-0.15	-0.19	-0.11	-0.14	-0.06
5500	-0.14	0.03	-0.19	-0.20	-0.14	-0.16	-0.11
5600	-0.16	0.16	-0.22	-0.21	-0.16	-0.17	-0.16
5700	-0.18	0.18	-0.24	-0.23	-0.19	-0.20	-0.20
5800	-0.20	0.13	-0.26	-0.26	-0.22	-0.23	-0.23
5900	-0.22	0.09	-0.28	-0.27	-0.25	-0.23	-0.24
6000	-0.24	0.06	-0.29	-0.28	-0.25	-0.22	-0.24
6100	-0.25	0.01	-0.30	-0.29	-0.24	-0.22	-0.24
6200	-0.27	-0.07	-0.31	-0.29	-0.25	-0.22	-0.26
6300	-0.29	-0.17	-0.33	-0.30	-0.28	-0.24	-0.29
6400	-0.31	-0.27	-0.34	-0.31	-0.32	-0.27	-0.32
6500	-0.32	-0.34	-0.35	-0.32	-0.35	-0.30	-0.34
6600	-0.34	-0.32	-0.36	-0.34	-0.36	-0.33	-0.36
6700	-0.35	-0.31	-0.37	-0.35	-0.37	-0.37	-0.37
6800	-0.37	-0.34	-0.37	-0.37	-0.37	-0.40	-0.38
6900	-0.38	-0.32	-0.38	-0.38	-0.37	-0.42	-0.39
7000	-0.40	-0.31	-0.39	-0.39	-0.38	-0.43	-0.40
7100	-0.41	-0.35	-0.39	-0.40	-0.39	-0.44	-0.40
7200	-0.42	-0.40	-0.40	-0.41	-0.40	-0.44	-0.40
7300	-0.43	-0.43	-0.42	-0.41	-0.40	-0.44	-0.40
7400	-0.45	-0.45	-0.43	-0.42	-0.40	-0.44	-0.40
7500	-0.46	-0.46	-0.45	-0.42	-0.39	-0.44	-0.40
7600	-0.47	-0.46	-0.46	-0.43	-0.39	-0.44	-0.40
7700	-0.48	-0.47	-0.46	-0.43	-0.39	-0.45	-0.41
7800	-0.49	-0.51	-0.47	-0.44	-0.38	-0.46	-0.41

or two orders of magnitude smaller than other nebulae (see Table II). It also has the largest apparent size (Table I). The present data of optical spectrum, however, do not offer any opportunity to compare the detailed dust properties within planetary nebulae.

Finally, the ratio of total to selective extinction defined as $R = A_V/E_{B-V}$ was derived using the reddening curve obtained by averaging the calculated reddening curves. There are two ways to determine R , color difference method and variable extinction method [12]. The color difference method, which is accessible with our data, requires the knowledge of the zero-point $A_\lambda = 0$ to evaluate A_V . Unless we have the information of absolute magnitude or distance for a given object, a direct determination of R is difficult. Since the extinction must vanish at $\lambda = \infty$, direct evaluation of A_V involves measurements at extremely long wavelengths. With the present data, the best we can do is to make an extrapolation in the long wavelength region.

The R value estimated from our data is around $1.5 \sim 2$, which is significantly small compared to the standard value of 3 [13]. Although there is a large uncertainty in our extrapolation, the small R is indeed what is expected directly from the visual inspection of Fig. 11. The mean trend of derived reddening functions increase E_{B-V} at least one and half times greater than that of normal Whitford law, and the flatness in the longest wavelengths makes A_V smaller (unless there are abrupt variations beyond infrared).

V. Discussion

Spectrophotometric data for six planetary nebulae in the direction of the galactic center were used to derive the properties of the interstellar reddening for this region. The data cover most of the visible spectrum, extending from [O II] λ 3727 to well beyond [S II] λ 6717, 6731. In order to evaluate the reddening law for the direction of each nebula, we pursued a new method in which the nebular continuum is employed. The observed nebular continuum was compared to the theoretically predicted continuum of the corresponding electron temperature, which was derived from the forbidden emission lines. The difference between the observed and theoretical continuum was assumed to be solely due to the interstellar reddening. Although there are some indications of the central stars in the case of O-1.6 and 6-3.3 (see Fig. 7(a) and Fig. 10(a) for the broad He II emission feature at X4686 which indicates Wolf-Rayet nucleus), these effects on the nebular continuum were regarded as negligible since the risings of continua at the ultraviolet wavelengths were not found.

The derived reddening function for each planetary nebula shows rather good agreement with the standard Whitford law in long wavelength region, whereas there exist significant deviations in ultraviolet. The mean reddening curve is characterized by steeper rising in ultraviolet and a little flatter in the longest wavelengths compared with the Whitford curve. This deviation may be explained by a different size distribution and/or a different composition of dust grains lying toward the galactic center. According to theoretical modeling of grains, the same trend can be simulated by changing the size parameter of so-called Type I grains (see Fig. 3 in [14]). However an extensive comparison with theories requires the observation around the ultraviolet bump at 2200Å.

The ratio of total to selective extinction, R , was also derived by a crude extrapolation of the mean reddening curve to $\lambda = \infty$. The ratio R is important figure for the determination of photometric distances since it involves $V_0 = V - A_V = V - R \cdot E_{B-V}$. Therefore

it has been of great interest to know not only the value of R but whether it is constant for different regions of the Galaxy. The derived value of $R = 1.5 \sim 2.0$ is much smaller than the standard ratio $R = 3$. The small R implies that the universal law of interstellar reddening does not work for the direction of galactic center. Photometric distances calculated with $R = 3$ would be then too small and the interstellar extinction too high for this region. The small value of R may result either from a different chemical composition or from a different size distribution of the interstellar grains. The conclusion, however, probably is too premature since the extrapolation employed to find the zero-point was not a reliable quality. The reddening curves are known to have abrupt changes at far-infrared wavelengths in many cases [12], which suggest the shape of the curve within $0 < \lambda^{-1} < 1$ should be directly measured before we can derive a reliable R value.

It is interesting, however, to notice an independent study [15] reporting small value of R in the direction of $l = 270'' \sim 360''$. Based on the comparison of kinematical parallaxes with spectroscopic and photometric data, they concluded that the ratio R varies from about 1.5 to about 4.0 along the galactic longitude with the minimum taking place at $l = 0^\circ$. The variation of R was later successfully simulated as a function of the size parameter for the composite and ice grains [16]. It is difficult to compare our result with any existing theories since the reddening function obtained here covers only visible wavelengths. Further extensive study with data covering much larger wavelength range is required to model the nature of interstellar dust toward the galactic center.

Acknowledgment

I acknowledge the partial support by the National Science Council of Taiwan under the grant NSC85-2112-M008-019.

References

- [1] L. Spitzer, *Physical Processes in the Interstellar Medium* (John Wiley & Sons, New York, 1978).
- [2] S. R. Potasch, *Planetary Nebulae* (D. Reidel, Dordrecht, 1984).
- [3] L. Perek and L. Kohoutek., *Catalog of Planetary Nebulae* (Czechoslovakia Academic of Science, Prague, 1967).
- [4] T. D. Kinman, M. W. Feast, and B. M. Lasker, *Astron. J.* 128, 325 (1988).
- [5] A. W. Rodgers, P. Conroy, and G. Bloxham, *Puhl. Astron. Soc. Pac.* 100, 626 (1988).
- [6] J. B. Oke and J. E. Gunn, *Astrophys. J.* 266, 713 (1983).
- [7] R. M. Pengelly, *Mon. Not. Roy. Astron. Soc.* 127, 145 (1964).
- [8] L. Binette, PhD Thesis, Australian National University (1982).
- [9] I. N. Evans, PhD Thesis, Australian National University (1986).
- [10] M. Brocklehurst, *Mon. Not. Roy. Astron. Soc.* 153, 471 (1971).
- [11] A. E. Whitford, *Astron. J.* 63, 201 (1958).
- [12] H. L. Johnson, in *Nebulae and Interstellar Matter*, eds. B. M. Middlehurst and L. H. Aller (Univ. of Chicago Press, Chicago! 1968), p.167.
- [13] C. W. Allen, *Astrophysical Quantities* (Athlone Press, London, 1973).
- [14] S. Isobe, *Publ. Astron. Soc. Japan* 25, 253 (1973).
- [15] M. Crézé, *Astron. Astrophys.* 21, 85 (1972).
- [16] M. Crézé, and S. Isobe. *Ann. Tokyo Astron. Obs.* 14. 270 (1975).